AGU **ADVANCING EARTH AND SPACE SCIENCE**

JGR Biogeosciences

Key Points:
- Climate-vegetation coupling in Europe is quantified by decomposing sub-seasonal greenness anomalies using grid-wise defined growing seasons
- Large-scale climate-vegetation coupling during the first two months of the growing season largely determines the full-year coupling
- The North Atlantic Oscillation, Scandinavian Pattern, and East Atlantic patterns emerge as the most relevant large-scale drivers for this coupling

Early Growing Season Anomalies in Vegetation Activity Determine the Large-Scale Climate-Vegetation Coupling in Europe

Minchao Wu[1] , Giulia Vico[2] , Stefano Manzoni[3] , Zhanzhang Cai[4] , Maoya Bassiouni[2] , Feng Tian[5] , Jie Zhang[1], Kunhui Ye[1] , and Gabriele Messori[1,6,7]

[1]Department of Earth Sciences, Uppsala University, Uppsala, Sweden, [2]Department of Crop Production Ecology, Swedish University of Agricultural Sciences (SLU), Uppsala, Sweden, [3]Department of Physical Geography and Bolin Centre for Climate Research, Stockholm University, Stockholm, Sweden, [4]Department of Physical Geography and Ecosystem Science, Lund University, Lund, Sweden, [5]School of Remote Sensing and Information Engineering, Wuhan University, Wuhan, China, [6]Centre of Natural Hazards and Disaster Science (CNDS), Uppsala, Sweden, [7]Department of Meteorology and Bolin Centre for Climate Research, Stockholm University, Stockholm, Sweden

Abstract The climate-vegetation coupling exerts a strong control on terrestrial carbon budgets and will affect the future evolution of global climate under continued anthropogenic forcing. Nonetheless, the effects of climatic conditions on such coupling at specific times in the growing season remain poorly understood. We quantify the climate-vegetation coupling in Europe over 1982–2014 at multiple spatial and temporal scales, by decomposing sub-seasonal anomalies of vegetation greenness using a grid-wise definition of the growing season. We base our analysis on long-term vegetation indices (Normalized Difference Vegetation Index and two-band Enhanced Vegetation Index), growing conditions (including 2m temperature, downwards surface solar radiation, and root-zone soil moisture), and multiple teleconnection indices that reflect the large-scale climatic conditions over Europe. We find that the large-scale climate-vegetation coupling during the first two months of the growing season largely determines the full-year coupling. The North Atlantic Oscillation and Scandinavian Pattern phases one-to-two months before the start of the growing season are the dominant and contrasting drivers of the early growing season climate-vegetation coupling over large parts of boreal and temperate Europe. The East Atlantic Pattern several months in advance of the growing season exerts a strong control on the temperate belt and the Mediterranean region. The strong role of early growing season anomalies in vegetative activity within the growing season emphasizes the importance of a grid-wise definition of the growing season when studying the large-scale climate-vegetation coupling in Europe.

Plain Language Summary Climate and terrestrial ecosystems interact and affect the global climate. Such a climate-vegetation relationship can be effectively quantified by using satellites to measure how leafy and active the vegetation is, and numerical indices reflecting large-scale climate patterns over a given region. Previous studies generally focused on changes in mean vegetation indices over the full growing season, which is usually defined by a fixed range of astronomical months for large geographical regions. This overlooks the fact that growing seasons differ in space and vegetation responds differently to the climate in different growing season periods. In this study, we explore how vegetation and climate interact within a growing season, here defined specifically for the local conditions. We find that there are strong relationships between the large-scale climate patterns and vegetation indices during the first two months of the growing season. Our findings highlight the important role of the vegetation activity during the early growing season for the year-to-year vegetation changes in Europe. Hence, for a better understanding of the climate-vegetation relationships, it is necessary to consider the spatial differences in the growing season, in particular for large geographical regions.

1. Introduction

The terrestrial carbon budget is coupled to atmospheric CO_2 concentrations (Friedlingstein et al., 2019; Keeling et al., 1995; Le Quéré et al., 2018; Piao et al., 2020; Zeng et al., 2005). Its future interplay with climatic conditions will likely have profound impacts on the evolution of the global climate under continued

anthropogenic forcing (Betts et al., 2004; Ciais et al., 2013; Friedlingstein et al., 2006). The terrestrial carbon budget and climate interact at multiple temporal and spatial scales (Friedlingstein et al., 2019; Le Quéré et al., 2018; Messori et al., 2019; Rödenbeck et al., 2018): there are very local effects, for example, hourly to seasonal small-scale direct drivers that affect respiration (Homyak et al., 2018; Jarvis et al., 2007; Talmon et al., 2011) and gross productivities (Law et al., 2002; Noormets et al., 2008; Novick et al., 2016) and subseasonal or longer effects at the regional to continental scales, for example, the coupling between large-scale vegetation greenness and teleconnection indices such as the El Niño – Southern Oscillation (ENSO) (Anderegg et al., 2015; Behrenfeld et al., 2001; Bowman et al., 2017; Z.M. Chen et al., 2004) or the North Atlantic Oscillation (NAO) (Gonsamo et al., 2012; Maignan et al., 2008; Nordli et al., 2008; Stöckli & Vidale, 2004). Partly due to this variety of scales, many aspects of the carbon cycle-climate coupling are poorly understood, both from an observational and modeling perspective (Piao et al., 2020).

Remotely-sensed observations are now providing data with extensive spatio-temporal coverage to address this challenge. Specifically, remotely sensed vegetation indices available at up to meter horizontal resolution on a daily basis (e.g., Normalized Difference Vegetation Index, NDVI) have been used as proxies for photosynthesis, to detect changes in phenology, to diagnose the ecosystem-climate relationship, and more (Barichivich et al., 2013; Bastos et al., 2016; Belmecheri et al., 2017; Gonsamo et al., 2016; Maignan et al., 2008; Ruiz-Pérez & Vico, 2020; e.g., Stöckli & Vidale, 2004). Long-term satellite vegetation products may also help to explore the large-scale climate-vegetation coupling, provided the temporal and spatial scales relevant to the specific questions being tackled are identified.

From the climate perspective, the responses of the terrestrial carbon cycle to climate variability have been assessed based on individual variables, such as temperature or precipitation, and more recently on so-called climate variability indices, or the closely related teleconnection indices (for an overview, see Messori et al. [2019]). These indices reflect recurring large-scale atmospheric and/or oceanic patterns over a given region, which typically correspond to a known set of climate anomalies in multiple variables over neighboring or remote regions (e.g., Hurrell & Clara, 2010), and are closely related to spatio-temporal features of the carbon cycle. For example, ENSO (Rasmusson & Wallace, 1983) modulates the terrestrial carbon cycle over large swaths of the tropics (e.g., Qian et al., 2008). Similarly, the onset of the growing season and annual mean leaf phenology over central and northern Europe are closely related to the impact of the NAO (Hurrell et al., 2001) on winter temperature and precipitation (Gonsamo et al., 2016; Gouveia et al., 2008; Maignan et al., 2008; Stöckli & Vidale, 2004). This, in turn, implies that the NAO may directly affect the seasonal onset of the carbon uptake and the net ecosystem carbon balance in these regions (Goulden et al., 1998; Richardson et al., 2010). However, the question of whether the NAO could exert similar impacts as for the seasonal onset on other growing season months, and if other teleconnection indices may have corresponding influences, remains open.

In Europe, the quantification of present-day and expected future changes in the carbon cycle is still uncertain (e.g., Morales et al., 2007; Reuter et al., 2017). Europe is representative of the Northern hemisphere terrestrial ecosystem diversity (Hickler et al., 2012), and large changes in ecosystem phenology have already been observed in recent decades (2013; Chmielewski & Rötzer, 2001; Fu et al., 2014; Jin et al., 2019; Piao et al., 2019). Despite the importance of sub-seasonal timescales and latitudinal gradients, many studies of the large scale climate-vegetation coupling focus on annual means and interannual variations, and/or consider a fixed growing season over large spatial areas, thereby ignoring the impact of local climate conditions (e.g., thermal, photoperiodic and hydrological conditions) and dominant species in determining growing-season variations. For example, within a relatively small region like the Swiss Alps, altitudinal gradients can lead to a difference of growing season onset by 3–4 days per 100 meters of elevation (Moser et al., 2010). The use of a fixed range of astronomical months to define the growing season over climatically and ecologically heterogeneous areas can confound climate-vegetation couplings, while the focus on interannual variability makes it impossible to resolve the role of sub-growing season phenological dynamics.

Here, we explore the sub-seasonal dynamics of climate-vegetation coupling across Europe, accounting for location-specific growing seasons. We specifically consider sub-seasonal monthly changes of vegetation greenness over 1982–2014 and their responses to local and large-scale climate variability. Our specific questions are: (i) what is the role of sub-seasonal vegetation activity in the overall year-to-year vegetation variability in Europe? And: (ii) which part of the growing season generally has a strong sub-seasonal

Table 1
Satellite-Based Vegetation Indices Used in This Study

	GIMMS3g	VIP15-v004
Vegetation Index used	NDVI	EVI2
Platform and sensors	1981/07–2000/10:	1982/01–1999/12:
	AVHRR-2 (NOAA 7,9,11,14)	AVHRR-2 (NOAA 7,9,11,14)
	2000/11–2015/12:	2000/02–2014/12:
	AVHRR-3 (NOAA 16–19)	MODIS-Terra (MOD09CMG)
Temporal coverage	1981/07–2015/12	1981/01–2014/12
Temporal resolution	15-day maximum	15-day maximum
Spatial resolution	1/12°	1/20°
Composite methods	Maximum value composite (MVC)	Constrained view angle maximum value composite (CV-MVC)
Key references	Pinzon & Tucker (2014); Tucker et al. (2005)	Didan (2010); Jiang et al. (2008); Pedelty et al. (2007)

Abbreviations: AVHRR-2, Advanced Very High Resolution Radiometer; CMG, Climate Modeling Grid; EVI2, Enhanced Vegetation Index 2; GIMMS3g, Global Inventory Modeling and Mapping Studies; NDVI, Normalized Difference Vegetation Index.

climate-vegetation coupling? To answer these questions, we consider teleconnection indices and vegetation indices based on different products, for a robust inference in the face of observational biases and uncertainties. The picture emerging from this analysis highlights which parts of the seasons are most relevant for the climate-vegetation coupling, for which additional investigations of the carbon budget variability can be most fruitful.

2. Data and Methods

2.1. Data

The 33-years overlap period 1982–2014 among all the datasets of interest was chosen for the analysis in this study unless otherwise specified.

2.1.1. Vegetation Indices From Satellite-Based Products

To detect the variability of vegetation greenness over Europe while maximizing the robustness of the analysis, we employed two vegetation indices (VI) from two satellite products: NDVI from GIMMS3g version 1 and EVI2 from VIP15 (see Table 1 for more details). Discrepancies between the datasets may arise from differences in sensor platforms (Tian et al., 2015), correction and calibration algorithms, and temporal composites of the satellite products.

2.1.1.1. GIMMS NDVI3g

The third generation Global Inventory Modeling and Mapping Studies (GIMMS3g) satellite product are based on the Advanced Very High Resolution Radiometer (AVHRR) sensors (AVHRR/2 and AVHRR/3) onboard the NOAA satellite series (NOAA 7,9,11,14, 16–19), sensing in the visible, near-infrared (NIR), and thermal infrared portions of the electromagnetic spectrum. NDVI derived from red and near-infrared radiance (Rouse et al., 1974) is based on the GIMMS3g system and is called GIMMS NDVI3g. This data set currently provides the longest available continuous record of NDVI (1981/07–2015/12) and has been widely used to study the interannual variation of the terrestrial carbon cycle (e.g., Barichivich et al., 2013; Bastos et al., 2016). The dataset is produced based on a 15-days maximum value composite (MVC) at an approximately 8 km horizontal resolution, with radiometric calibration for improved snowmelt detection and aerosol correction (Pinzon & Tucker, 2014; Vermote et al., 1997).

2.1.1.2. VIP15v004 EVI2

Enhanced Vegetation Index 2 (EVI2), developed by the multi-sensor Vegetation Index and Phenology (VIP) Earth science data records project, is a two-band enhanced vegetation index without a blue band. It is derived based on the AVHRR and MODIS sensors (switching in 2000) and uses a MODIS-based red-NIR-MIR

model. EVI2 backward-extends the three-band EVI, which was designed to improve vegetation signal sensitivity in high biomass regions. EVI2 is functionally equivalent to EVI (Jiang et al., 2008), with similar performance and lower aerosol noise, and employs a hybrid per-pixel algorithm to ensure continuity between the different sensors during the transition period (i.e., the year 2000). EVI2 has been widely used to characterize land surface phenological dynamics, including LAI estimation (Kang et al., 2016; e.g., Liu et al., 2012), burn severity (Rocha & Shaver, 2009), and insect-induced defoliation (Olsson et al., 2016), complementing the long-term AVHRR-based NDVI and the relatively short-term MODIS-based EVI. The dataset version 4 VIP-EVI2 adopts a two-step filtering approach for the input daily data and incorporates the vegetation background signal, which aims to improve vegetation seasonal dynamics and spatial consistency for high-latitude boreal regions.

2.1.2. Growing Conditions

Three local growing conditions: 2m temperature, downwards surface solar radiation, and root-zone soil moisture were used to investigate the local climate-vegetation coupling. We extracted 2m temperature and downwards surface solar radiation from ECMWF's ERA5 reanalysis (Hersbach et al., 2020). We used monthly-mean data at approximately 31 km horizontal resolution over the same period as that of EVI2. We used root-zone soil moisture estimates from the Global Land Evaporation Amsterdam Model (GLEAM), which considers detailed physical and vegetation processes affecting total evapotranspiration and thus soil moisture variations (Martens et al., 2017; Miralles et al., 2011). The data version GLEAM v3.3a used in this study covers the period 1980–2018 at a monthly scale and 0.25° horizontal resolution. It is based on ERA5 forcing, and satellite and gauge-based observations (precipitation, vegetation optical depth, soil moisture, etc.).

2.1.3. Teleconnection Indices

Seven teleconnection indices obtained from NOAA Center for Weather and Climate Prediction (see Data Availability) were selected to reflect large-scale European climate variability. These are the NAO, East Atlantic Pattern (EA), West Pacific Pattern (WP), Pacific/North American Pattern (PNA). East Atlantic/West Russia Pattern (EA/WR), Scandinavian Pattern (SCA), and Polar/Eurasian Pattern (POL).

2.1.4. Ancillary Data

To define the grid-wise growing season, we used monthly frost day frequency at 0.5-degree horizontal resolution from CRU TS404 (Harris et al., 2020). For the analysis of climate-vegetation coupling, we further used the MODIS landclass data set MCD12C1 (Friedl et al., 2002) and the Köppen-Geiger climate classification (Kottek et al., 2006) for regrouping of spatial data (see Methods below). The MODIS landclass data set provides yearly land cover types in 0.05-degree resolution Climate Modeling Grid (CMG) cells and contains 17 International Geosphere–Biosphere Program (IGBP) land cover classes.
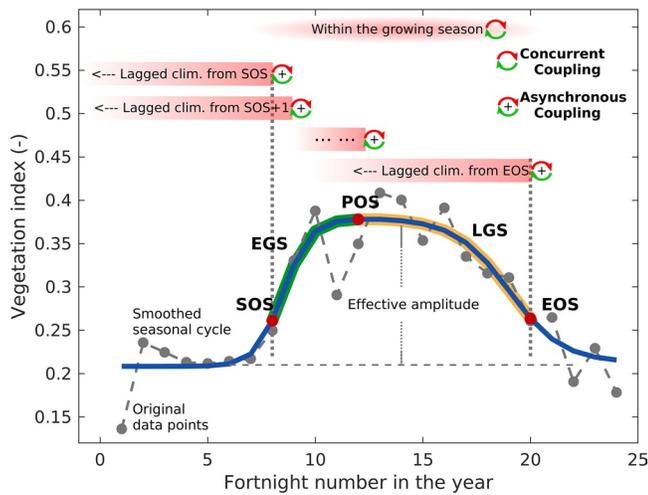
2.2. Methods

Figure S1 presents the data workflow and data processing from the VI and climate datasets used as inputs to the results of our analysis, including the locally defined growing season.

2.2.1. Spatial Resampling and Grouping

To reduce noise induced by small-scale land surface heterogeneities (e.g., topography) that may affect the large-scale climate-vegetation coupling, and to maintain cross-data consistency for analysis, we resampled all the gridded datasets to 0.5-degree horizontal resolution.

For the MODIS landclass data set, each coarse-grained gridpoint was assigned the land class corresponding to the maximum ratio of the resampling grids. The resampled land classes were then aggregated into eight groups, highlighting common vegetation characteristics for specific land surfaces over Europe. Those eight groups and their corresponding IGBP land classes are group EF for the evergreen forest; group DF for the deciduous forest; group MF for the mixed forest; group WS for closed shrubland, open shrubland, and woody savannas; group GRS for grasslands and savannas; group WL for wetland; group CRP for crop land and natural vegetation mosaic; group SIB for snow, ice, barren soil, and sparse vegetation.

Figure 1. Schematic diagram of the characterization of the growing season (GS) for each gridpoint, including the definitions of phenological parameters (red dots): the start of the growing season (SOS), the end of the growing season (EOS), the peak of the growing season (POS), the early growing season (EGS), and the late growing season (LGS). The climate-vegetation coupling during the growing season is characterized in two ways: (i) concurrent coupling (red and green arrows without plus sign); and (ii) asynchronous coupling (red and green arrows and a plus sign) with specific teleconnection indices in the months preceding each growing season month (i.e., lags of the teleconnection indices relative to the VI by 1–5 months). Gray dots represent the original VI data points, while the blue curve represents the smoothed seasonal cycle.

To distinguish vegetation responses to the prevailing thermal and hydrological conditions, we define three climate zones based on the Köppen-Geiger climate classification (Kottek et al., 2006), as (1) the boreal zone (Köppen-Geiger climate zones: Dfb, Dfc, ET); (2) the temperate zone (Köppen-Geiger climate zones: Cfa, Cfb, Cfc); and (3) the Mediterranean zone (Köppen-Geiger climate zones: Csa, Csb, Csc, BSk). The spatial patterns of the grouped land classes and climates are shown in Figure S2.

2.2.2. Time-Series Smoothing and Temporal Aggregation of Vegetation Indices

In addition to the temporal compositing methods (e.g., MVC) and corrections applied in the original VI data set, TIMESAT version 3.3 (Jönsson & Eklundh, 2004) was used to post-process the VI time-series data to further eliminate atmospheric effects and construct high-quality VI time-series. First, the seasonal and trend decomposition (STL) spike filter was applied to reduce the influences of outliers. Double logistic function fitting was then applied to smooth the VI time-series and further minimize the influence from noise (Figure S3). Parametric smoothing approaches may be difficult to apply over a large-scale domain when ground reference data are lacking and the optimal parameter setting is unknown. The double logistic filter can minimize the fitting uncertainty because it does not rely on smoothing parameters. This approach has been reported to yield a robust fitting close to the ground measurements and performs well for the high-latitude ecosystem, where low-quality retrievals or data gaps usually occur (Beck et al., 2006; Cai et al., 2017; Gao et al., 2008). The smoothed bi-weekly VI data were then aggregated at a monthly temporal frequency.

2.2.3. Definition of the Growing Season and Its Subperiods

Based on the smoothed VI time series, we defined grid-wise climatological growing seasons for Europe through a set of key phenological parameters, which include the start of the growing season (SOS), the peak of the growing season (POS), the end of the growing season (EOS), and the length of the growing season (LOS; Figure 1). We detected phenological cycles for the actual growing season based on an effective greenness amplitude VI_{eff}, defined as the difference between the maximum and minimum VI within a seasonal cycle; i.e., $VI_{eff} = VI_{max} - VI_{min}$. Following Reed et al. (1994), Jeong et al. (2011) and Jönsson and Eklundh (2004), and considering potential frost damage to vegetation during the start and the end of the growing season (e.g., Augspurger, 2009), we extracted SOS and EOS using the detected phenological cycle and the monthly frost day frequency. Specifically, SOS is defined as the month when incremental vegetation greenness during the green-up phase (i.e., the part of the smoothed curve with a positive first derivative) reaches at least 15% of VI_{eff} and more than 15 days are frost-free. Similarly, EOS is defined as the month before the month when the decreasing greenness (i.e., the part of the smoothed curve with a negative first derivative) falls below 15% of VI_{eff} and fewer than 15 days are frost-free. POS is defined as the average of the months with at least 85% of VI_{eff}. LOS is the number of months between SOS and EOS.

We then divided the growing season into two subperiods: (1) the early growing season (denoted as EGS) is defined as the period between SOS and POS, and (2) the late growing season (denoted as LGS) is defined as the period between POS and EOS. The subdivision of the year into a growing season and its two subperiods are exemplified in Figure 1. This approach aims to capture phenological changes within a single growing season and emphasizes long-term phenological variation. Ecosystems with multiple growing seasons, such as croplands with the main crop and a cover crop, or abrupt phenological changes due to extreme events, are characterized by phenological patterns that cannot be analyzed with this approach, and these biomes are out of the scope of this study. Figure S4 shows that SOS, EOS, and LOS exhibit a general southwestern-northeastern gradient throughout the continent. It is worth noting that the growing season in the Mediterranean region is successfully characterized by our approach. In that region, the SOS occurs in November, at the beginning of the rainy season, and the EOS occurs in July (Figures S4a and S4b)—a pattern

in antiphase with the seasonal cycle in the boreal and temperate regions (Figure S3). This is in contrast to simpler approaches based on a single climatic threshold (e.g., temperature), which do not allow detecting the growing season for regions where growing season onset is controlled by the co-occurrence of multiple climatic conditions (Linderholm, 2006).

2.2.4. Definition of the Growing Season Anomalies

The monthly anomalies were generated based on the time-series detrended with a 5-year running mean and deseasonalized by subtracting the average seasonal cycle and were calculated only during the identified growing season period. The year-to-year VI anomalies of each identified growing season month (m) in a given gridpoint and year y are denoted as $\alpha_{GS}(m,y)$. These anomalies are then normalized by the mean vegetation greenness to obtain the equivalent of a coefficient of variation (CV). Accordingly, the interannual stability of monthly growing season VI is calculated as:

$$CV_{GS}(m) = \frac{\sigma_y\left(\alpha_{GS}(m,y)\right)}{\mu_{GS}} \tag{1}$$

where σ_y is the standard deviation of the year-to-year VI anomalies for month m, and μ_{GS} is the long-term vegetation greenness for the entire growing season. The CV of the entire growing season is then given by:

$$CV_{GS} = \frac{\sigma_y\left(\frac{\sum_{m=SOS}^{EOS}\alpha_{GS}(m,y)}{LOS}\right)}{\mu_{GS}}, \tag{2}$$

where σ_y represents the standard deviation of the year-to-year mean growing season anomalies. The relative importance of VI anomalies of each growing season month to the entire growing season for year y is defined as:

$$\gamma_{GS}(m,y) = \frac{\left|\alpha_{GS}(m,y)\right|}{\sum_{m=SOS}^{EOS}\left|\alpha_{GS}(m,y)\right|} \tag{3}$$

The relative importance of growing season month stability to the stability of the entire growing season is given by:

$$\lambda_{GS}(m) = \frac{CV_{GS}(m)}{CV_{GS}} \tag{4}$$

where $\lambda_{GS}(m)$ can be >1, indicating high sub-seasonal instability, and possible compensating effects within the growing season (e.g., positive anomalies for some months but negative for others) that buffer the overall growing season interannual variability. Similarly, the relative importance of EGS and LGS variability to that of the entire growing season, λ_{EGS} and λ_{LGS}, are written as:

$$\lambda_{EGS} = \frac{CV_{EGS}}{CV_{GS}} \tag{5}$$

and

$$\lambda_{LGS} = \frac{CV_{LGS}}{CV_{GS}} \tag{6}$$

where:

$$CV_{EGS} = \frac{\sigma_y \left(\dfrac{\sum_{m=SOS}^{POS-1} \alpha_{GS}(m, y)}{POS - SOS} \right)}{\mu_{GS}} \tag{7}$$

$$CV_{LGS} = \frac{\sigma_y \left(\dfrac{\sum_{m=POS}^{EOS} \alpha_{GS}(m, y)}{EOS - POS + 1} \right)}{\mu_{GS}} \tag{8}$$

As in Equation 2, in Equations 7 and 8, σ_y indicates the standard deviations of the year-to-year anomalies, and anomalies are averaged over the early and late growing season, respectively. Based on Equations 5 and 6, the relative difference of the coefficients of variation during EGS and LGS is calculated as:

$$\Delta\lambda = \lambda_{EGS} - \lambda_{LGS} \tag{9}$$

When $\Delta\lambda > 0$, early growing season variability dominates, and vice versa for negative values.
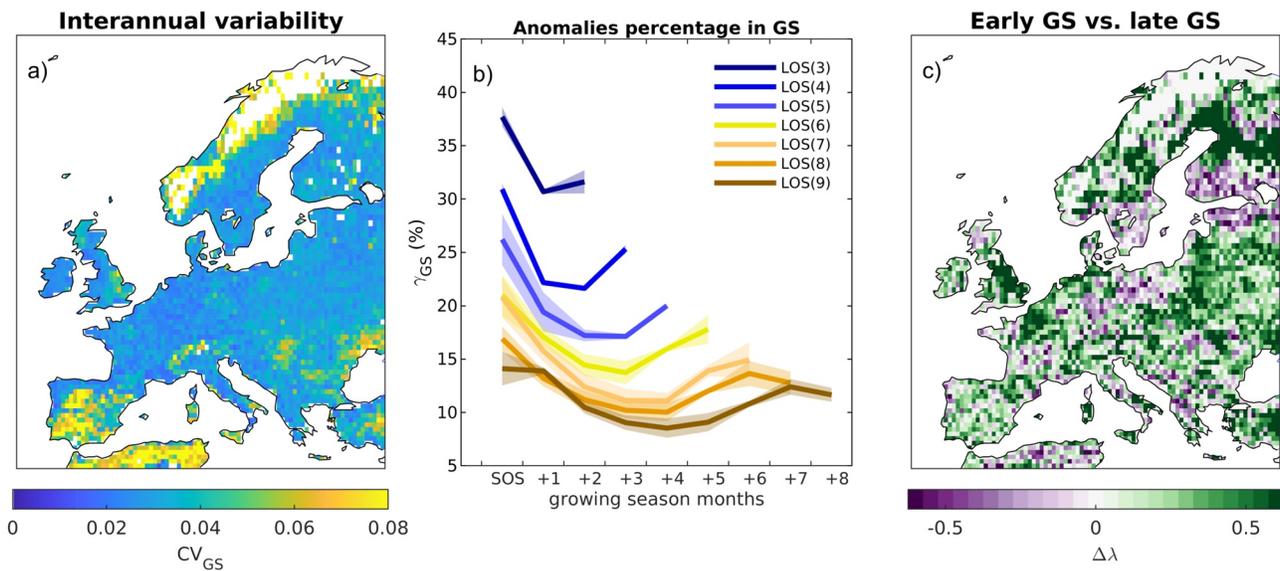
2.2.5. Coupling of Vegetation Index Anomalies and Local Growing Conditions and Teleconnection Indices

Based on the generated phenological parameters used to characterize the growing season (see *Definition of the growing season and its subperiods*), climate anomalies for each growing season month were also extracted. For each gridpoint, climate variables and teleconnection indices are timed relative to the locally identified growing season (see Figure 1). Their year-to-year anomalies are denoted as $\beta_{GS}(m, \theta)$, in which θ is the negative lag in months of the climate data relative to the VI at growing season month m. For local growing conditions, we focus on concurrent effects, and therefore set $\theta = 0$. For the teleconnection indices, we additionally consider lagged effects, where the teleconnection index precedes the phenological month by 1–5 months. In this case, θ thus varies in the range −5 to 0. When $\theta < 0$, the coupling of $\beta_{GS}(m, \theta)$ with $\alpha_{GS}(m)$ is referred to as asynchronous coupling. For example, $\beta_{GS}(1, -2)$ refers to the anomaly of a teleconnection index two months before SOS.

For concurrent coupling, we used the partial correlation coefficient (ρ) to associate VI anomalies with the three local growing conditions (2m temperature, solar radiation, and soil moisture; see *Growing conditions and land surface classes*). Such an approach allows isolating the association between vegetation and each local growing condition while considering possible confounding effects from the other two growing conditions. For the asynchronous coupling, we used Pearson's correlation coefficient (r) to associate VI anomalies with seven teleconnection indices at different time lags (see *teleconnection indices*). That is, for each time-series of VI anomalies for a specific growing season month and gridpoint, there will be seven (number of teleconnection indices) times six (number of time lags including zero-lag) pairs of time-series to be correlated. Such an approach does not eliminate possible influences from the covariance between different teleconnection indices, but can nonetheless give a general indication of the climate-vegetation coupling across different temporal scales due to different large-scale circulation patterns. In this way, the dominant teleconnection index for a specific lag, growing season month, and gridpoint can be found. The strongest asynchronous coupling which reveals the most relevant large-scale climate control is then given by:

$$\Phi_{max} = \max\left(\left| r(m, k, \theta) \right| \right) \tag{10}$$

where k denotes individual teleconnection indices.

Figure 2. Interannual variability of vegetation greenness as represented by vegetation indices and the importance of early growing season variation over Europe for the period 1982–2014. (a) Spatial distribution of the coefficient of variation (CV_{GS}, Equation 2) for the growing season (GS) mean vegetation index (VI), averaged across NDVI-based and EVI2-based VI products. (b) Relative contribution of absolute monthly greenness anomalies to the total absolute anomaly for the entire growing season ($\gamma_{GS}(m, y)$, Equation 3). Values represent the spatial averages over areas with a given length of the growing season (LOS, indicated by colors). The shadings represent the differences between NDVI-based and EVI2-based data, and the solid lines represent the mean of the two products. (c) Relative difference between early- and late-growing season variations ($\Delta\lambda$, Equation 9). Calculated values are the mean from the two remote-sensing products. White indicates no data, no growing season due to invalid data points, or weak relative difference.
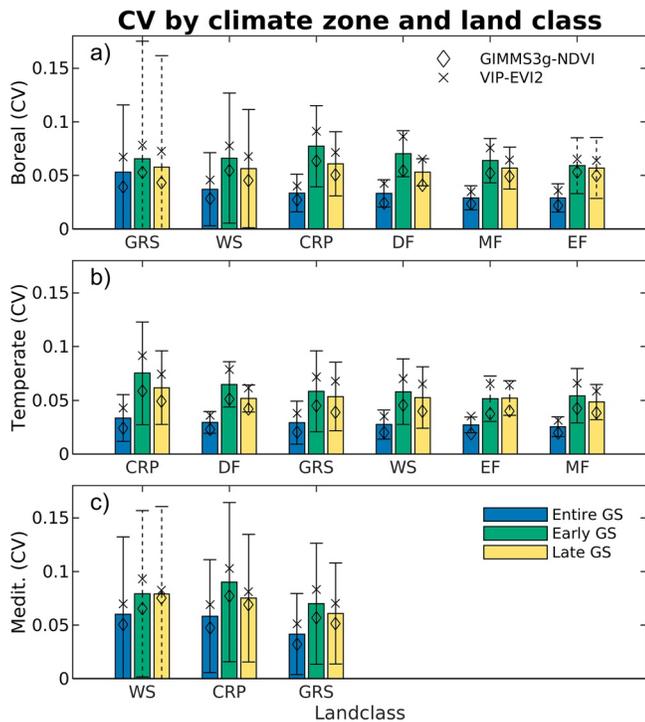
3. Results

3.1. Early Growing Season Dominates the Variation in Vegetation Indices

The Iberian peninsula, North Africa, the regions surrounding the Black Sea and the Scandinavian mountains have the largest growing season CV in Europe (Figure 2a), indicating a large interannual variability of the vegetation greenness during the last three decades. The contribution of the different growing season months to the total growing season mean anomaly is not uniform: the highest contributions come from the months corresponding to the SOS and soon after that, while the lowest contributions come from the months around the POS (Figure 2b). For LOS of 3–7 months, there are relatively higher contributions from the first several months, lower values for the mid growing season months, and again an increase for the last several months, albeit with a smaller amplitude compared with the early-mid growing season difference. A similar pattern can be found for the changes in the CV of individual growing season months ($CV_{GS}(m)$, Equation 1, Figure S5). Comparing the early growing season greenness anomalies with those of the late growing season, the dominance of the former emerges over western Europe, parts of central Europe, southern and eastern Europe, and the majority of Scandinavia (Figure 2c). In contrast, North Africa with highly variable vegetation activity (high CV_{GS}), and the Gulf of Finland, southern Sweden, and central Germany with less variable vegetation (low CV_{GS}) are dominated by the late growing season variations. The early-late growing season differences decrease with increasing LOS and become marginal for LOS = 9 months, which corresponds to parts of western Europe and the southern Iberian peninsula (Figure S4c). This pattern is independent of the chosen VI data set. Indeed, differences between NDVI and EVI2 are smaller than the amplitude of the early-late growing season differences, even though they can be large for specific growing season months (shading in Figure 2b).

3.2. Contribution of Vegetation Index Anomalies in the Early Growing Season Across Land Classes and Climates

The boreal and Mediterranean regions tend to have larger variations in growing season mean greenness than temperate regions (blue bars, Figure 3). In each climate zone, herbaceous vegetation and areas with
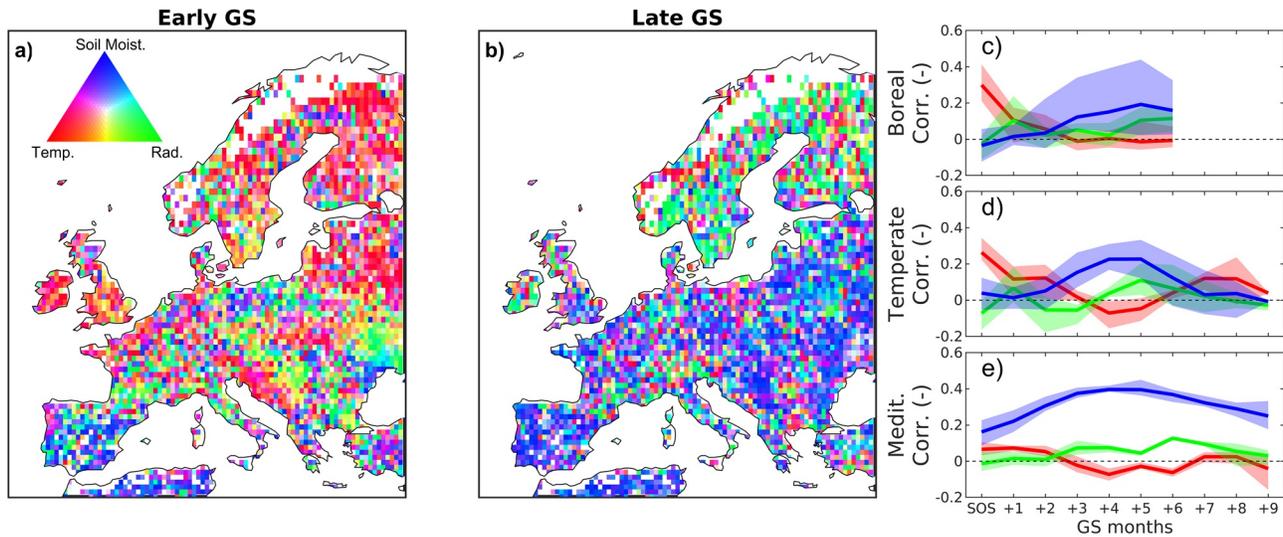
Figure 3. Comparison of coefficients of variation in the early growing season (CV_{EGS}) and late growing season (CV_{LGS}) by climate zone and land class (see Figure S2 for the definition of climate zones and land classes). Error bars indicate the standard deviation of CV across spatial points within each category. The calculation was based on the mean of NDVI-based and EVI2-based VI within the analysis period. Symbols indicate the mean CV of each category for the two remote-sensing products. Gridpoints with a land classification that changed over the analysis period are excluded. Solid error bars indicate significant differences (Student's t-test, $p < 0.05$) between the mean CV_{EGS} and CV_{LGS}; dashed error bars indicate no significant differences. Landclasses in each climate zone are ordered by descending CV_{GS}. The y-scale varies across panels. CRP, crop land, and natural vegetation mosaic; DF, deciduous forest; EF, evergreen forest; GRS, grasslands, and savannas; MF, mixed forest; WS, closed shrubland, open shrubland, and woody savannas.

sparse tree cover (i.e., grassland, savannas, and croplands) are more variable than closed-canopy forests (i.e., deciduous forest, mixed forest, and evergreen forest). Deciduous forest in the temperate zone is an exception (Figure 3b), as it tends to have higher interannual variability than grassland and shrubland. A comparison of CVs within each climate zone and land cover class confirms that in most cases the early growing season variations are significantly (at $p > 0.05$) larger than the later growing season variations (green and yellow bars respectively, Figure 3). However, a land-class dependence can be easily identified. For example, evergreen forest tends to have little early-to-late growing season differences in both the boreal and the temperate zones (Figures 3a and 3b). Climate effects can also be identified, for example for shrublands and woody savannas. The early-to-late growing season difference for WS is not statistically significant for the Mediterranean area but becomes pronounced in the temperate-boreal regions, with relatively large spatial heterogeneity in the former. These patterns of relative differences across land classes and climate zones are generally consistent between EVI2 and NDVI, although the variability of EVI2 is higher than that of NDVI and the underlying reason is not clear.

3.3. Local Drivers of Climate-Vegetation Coupling

In the early growing season, temperature imposes a strong positive control in terms of high positive ρ between temperature and VI anomalies over the boreal and temperate western Europe, Finland, and parts of eastern Europe, in particular during the first two months of the growing season (Figures 4a and 4d), and for the majority of land classes (Figures S7a–S7l). Impacts from radiation and soil moisture are more geographically scattered, except for the Iberian peninsula, North Africa, and the cropland region north of the Black Sea. Over the latter region, a marked negative impact from radiation is found (Figure S6c). During the late growing season, soil moisture dominates over a large part of the continent with a strong positive effect, but weakening toward the EOS with relatively large landclass differences (Figures 4b–4d). Cropland and deciduous forest are the two landclasses with the strongest soil moisture control (Figures S7a–S7l). In addition, radiation and temperature together largely control the higher-latitude regions, including Scandinavia, parts of the British Isles and most of the Alps (Figure 4b). Moreover, GIMMS NDVI is more sensitive to radiation over these regions than the VIP vegetation indices (Figure S8). It is interesting to note that, even over boreal mesic regions such as Scandinavia, a weak negative temperature-vegetation coupling is found (Figure S6b), implying that a warm summer can suppress forest productivity there (Ruiz-Pérez & Vico, 2020; Solberg, 2004). Over the temperate regions, the correlation with temperature rises during the late growing season and in some cases dominates at the EOS, for example, in evergreen forests (Figures 4d and S7h–S7l). Over the boreal regions, radiation and soil moisture instead control the late growing season (Figures S7a–S7f).

For the Mediterranean, and in particular, for the Iberian peninsula and North Africa, soil moisture dominates vegetation growth throughout the entire growing season, with the strongest control during the mid-growing season, while the effects from radiation and temperature are mild (Figures 4e, S6e, and S6f). Such a response may be related to the dominant plant types, which mostly encompass low vegetation, such as grasslands, savannas, cropland, and shrubland (Figures S2a and S7m–S7o) that exhibit leaf senescence when soil moisture decreases (Jongen et al., 2011).
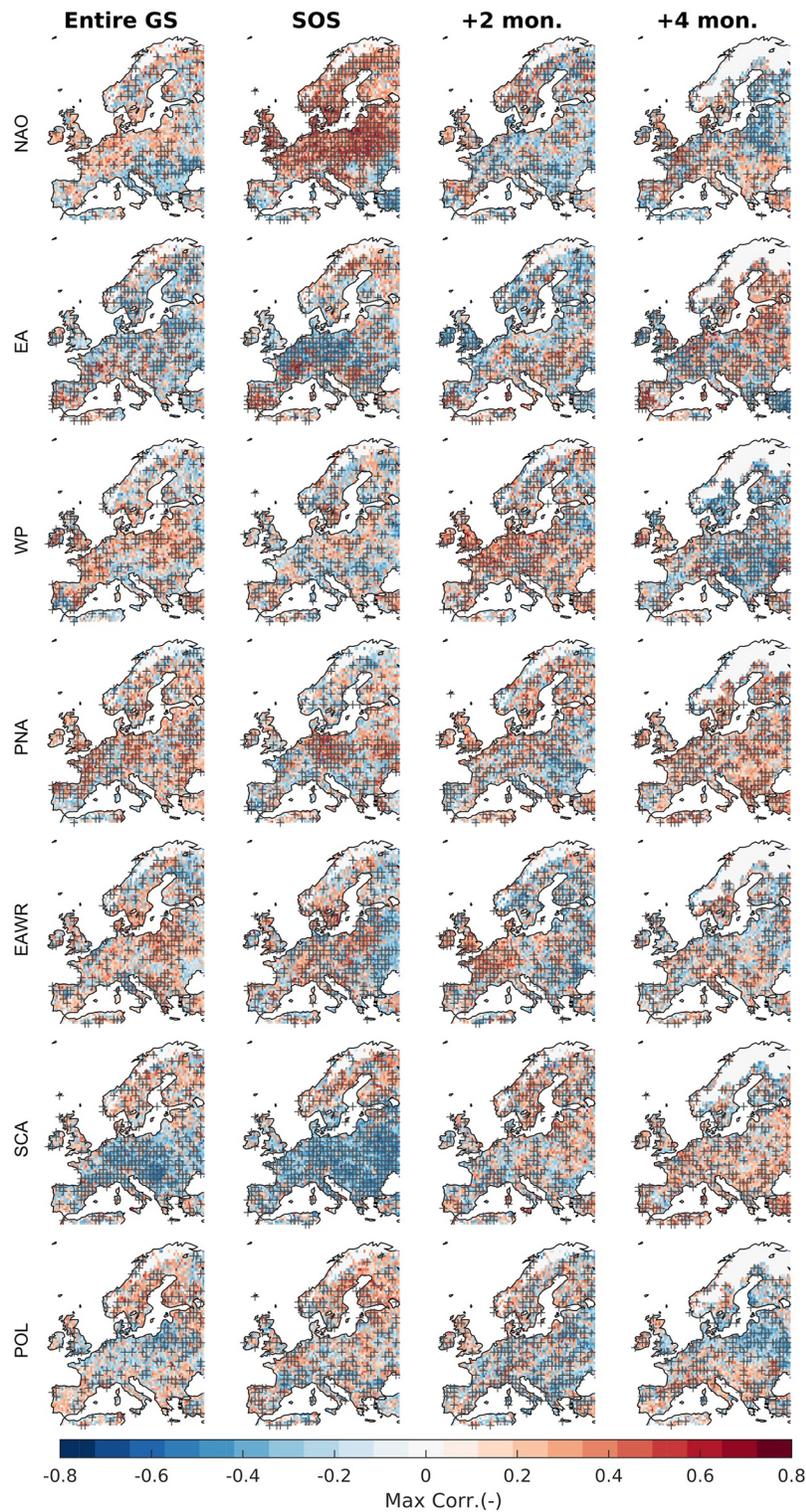
Figure 4. Concurrent climate-vegetation coupling for the early (a) and late (b) growing-season, based on partial correlation coefficients (ρ) between growing-season monthly EVI2 anomalies and concurrent local 2m temperature (red), downwards surface solar radiation (green), and root-zone soil moisture anomalies (blue). The partial correlation was performed between pairs of time series of VI anomalies and one of the growing condition anomalies while controlling for the effects of the other two growing condition variables (see also Figure S6). (a)-(b) Spatial distribution of multi-driver sensitivities represented by Maxwell's color scheme (Agoston, 1987). This uses the weighted vector defined as [|ρ1|, |ρ2|, |ρ3|]/max(|ρ1|,|ρ2|,|ρ3|) to visualize the relationships among multiple divers, where ρ1, ρ2, and ρ3 are the three partial correlations of the three climate drivers, respectively. White indicates no data or non-identifiable growing season due to invalid data points. (c)-(e) Evolution of the monthly multi-driver sensitivities within the growing season for different climate zones (characterized by different growing season lengths); colors represent the three drivers as in (a)-(b). The shadings represent the range across land classes (see also Figure S7). EVI2, Enhanced Vegetation Index 2.

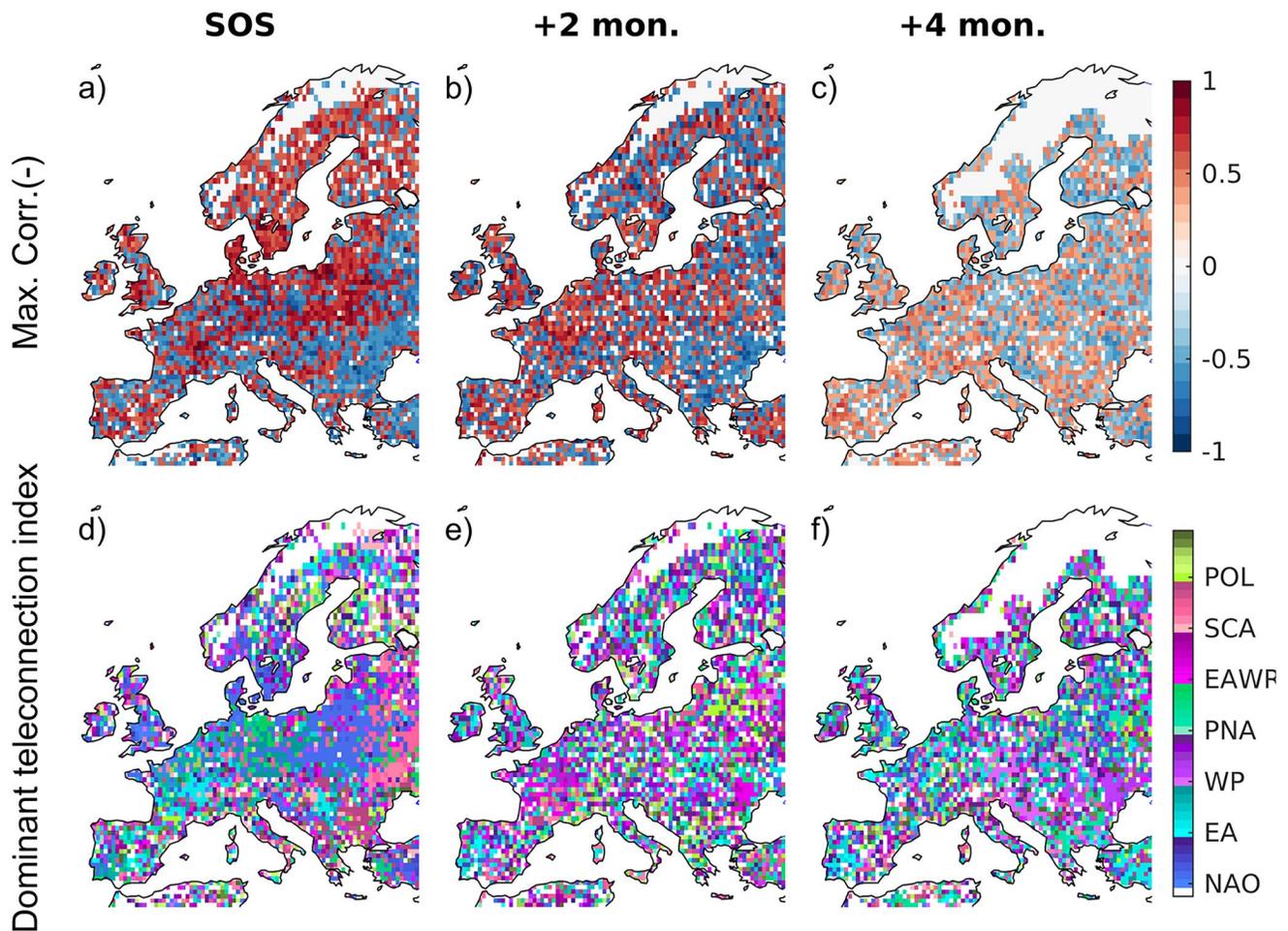### 3.4. Large-Scale Climate Coupling Dominated by Early Growing Season Dynamics

When identifying maximum correlations across lags of 0–5 months, the NAO exerts strong positive control over mid- and high-latitude Europe at the SOS. The initially positive correlation decreases starting from the second month within the growing season (SOS +1), and changes sign later in the season (Figure 5, top; Figures 6, 7a, and 7b). The strength of the correlation peaks at lags of 1–2 months. Simultaneous correlations between the early-growing season NAO (i.e., lag 0) and the early-growing season phenology are relatively weak (Figures 7a and 7b). The correlation coefficients based on the entire growing season anomalies present very similar spatial patterns to those from the first month of the growing season, albeit with lower values (Figure 5, first vs. second column).

In the temperate and boreal zones, the SCA at lag +2 months plays a role comparable in strength with that of the NAO at lags of 1–2 months during the early growing season, yet with an opposite sign (Figures 7a and 7b). Its footprint spans central and southern Europe, spatially complementing the NAO dominance (Figure 5, sixth row). Similar to the NAO, the impacts of SCA prevail during the first two growing season months, in which the spatial pattern generally reflects that of the entire growing season, and weakens in the following growing season months. The impacts of SCA and NAO exhibit a short-distance dipole between the Baltic Sea and the Black Sea regions (Figure 5, first vs. sixth row). Early growing season phenology, in particular for SOS and SOS+1, over central temperate Europe is negatively affected by EA, albeit at longer negative lags than for the NAO and SCA (Figures 5 and 7b). A 5-months lag relative to the SOS of this region (April to May), corresponds to the winter months (November to December).

For the Mediterranean zone, the overall response to large-scale climate variability modes is weak and spatially heterogeneous (Figures 5, 6, and 7c). The western and southwestern Iberian peninsula is an exception, and displays a constant positive EA control throughout the entire growing season (Figure 5, second row; Figures 6d–6f).

Figure 5. Spatial distribution of the maximum strength of the climate-vegetation coupling for individual teleconnection indices. The coupling is represented by Pearson's correlation coefficient (r) between growing season-based teleconnection indices (see Section 2) and subseasonal vegetation index anomalies (EVI2) within the growing season (GS). For each gridpoint, r with maximum absolute values across the different temporal lags (0–5 months, see Methods) are shown (see Equation 10). For example, the red area in the panel showing correlations at the SOS for NAO is attributed to the strong positive r from NAO_{lag1} and NAO_{lag2} as shown in Figures 7a and 7b. Gridpoints with significant r ($p < 0.05$) are stippled with "+". EA, East Atlantic Pattern; EA/WR, East Atlantic/West Russia Pattern; NAO, North Atlantic Oscillation; POL, Polar/Eurasian Pattern; PNA, Pacific/North American Pattern; SCA, Scandinavian Pattern; WP, West Pacific Pattern;. White indicates no data, no growing season due to invalid data points, or weak correlation.
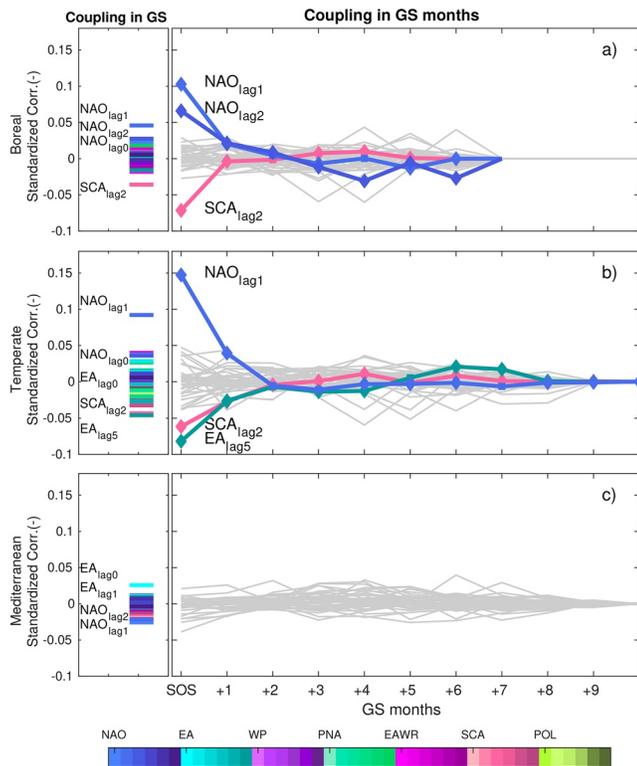
Figure 6. Changes in the spatial distribution of maximum strength (Φ_{max}; Equation 10) of the climate-vegetation coupling with corresponding Pearson's correlation coefficient (r) (a–c) and the corresponding dominant time-lagged teleconnection indices (d–f) within the growing season. Growing season vegetation index anomalies are based on EVI2. The different shades within each teleconnection index in panels (d–f) correspond to different lags (lightest shade 0 lag, darkest shade 5-months lag). The abbreviations of the teleconnection indices are as in Figure 5. EVI2, Enhanced Vegetation Index 2.

4. Discussion

We showed that sub-seasonal vegetation anomalies are important for the interannual variability in vegetation indices. Further, we defined a spatially varying growing season for Europe and showed that the early part of the growing season is key in determining the coupling between the large-scale climate variability and vegetation variability across the whole growing season. This is likely associated with the dominance of early-growing season greenness variability relative to that of the entire growing season (Figure 2) and its high sensitivity to specific large-scale circulation patterns. Indeed, the spatial analysis of the coupling between large-scale teleconnection indices and vegetation greenness reveals a strong control by the NAO, SCA, and EA over large parts of Europe during the first two months of the growing season (i.e., SOS and SOS+1; Figures 5–7). As the growing season progresses, the coupling weakens and the spatial patterns become more heterogeneous.

Our results underscore the importance of defining the growing season locally when investigating large-scale vegetation variability using remotely sensed VI products. Selecting a predetermined growing season based on astronomical months can miss its initial part which, as we have shown, is the most important for the climate-vegetation coupling. The spatially-varying growing season we defined here generally matches that based on the phenological data from the International Phenological Gardens network (Rötzer &

Figure 7. Seasonal average (left column) and seasonal evolution (right column) of the strength of asynchronous climate-vegetation coupling for different climate zones. The climate-vegetation coupling is expressed by Pearson's correlation coefficients (r) between teleconnection indices and VI anomalies as in Figure 5, but now aggregating the values of all gridpoints and standardizing by the total number of gridpoints within the corresponding climate zones. Only gridpoints with significant r ($p < 0.05$) for the respective teleconnection index are included in the calculation. Lines that do not extend beyond an absolute value of 0.06 are shown in gray. Diamond markers indicate an average of $|r|$ among significant gridpoints in the range 0.4–0.6, and square markers in the range 0.2–0.4. For each teleconnection index, the lightest shades indicate 0 lag and darkest shades 5-months lag; the abbreviations of the teleconnection indices are as in Figure 5.

Chmielewski, 2001), and FAO's growing season definition for crops using the SPOT-VEGETATION NDVI data set (FAO, 2020).

Our finding that early growing season greenness anomalies dominate annual VI variability over vast parts of Europe agrees with observations from phenological gardens across Europe, where marked interannual changes in the timing of growing season onsets and spring phase phenology (e.g., leaf unfolding, flowering) were found, while changes in the autumn phase phenology (e.g., leaf coloring and senescence) were generally limited (Chmielewski & Rötzer, 2001; Gordo & Sanz, 2009; Menzel & Fabian, 1999; Menzel et al., 2006; Thompson & Clark, 2008). For example, for the period 1943–2003 changes in the advancement of leaf unfolding, flowering, and fruiting (−0.48, −0.59, and −0.32 days yr^{-1}, respectively) were 4–5 times faster than in leaf falling (+0.12 days yr^{-1}) across Spain (Gordo & Sanz, 2009). The temperature sensitivity was also much larger for the first part of the growing season than for the latter (2.5 days/degree vs. 1.0 day/degree, Menzel et al., 2006) in Europe. This is generally in line with our findings, which show a larger partial correlation coefficient between vegetation greenness and temperature occurring during the early growing season than the late growing season over most of Europe (Figure 4).

The underlying drivers of the large early growing season anomalies and low mid and late-growing-season anomalies remain elusive, but a number of hypotheses can nonetheless be proposed. Early-growing season anomalies can be caused by the reduction in tolerance to low temperatures after the release of winter dormancy (Lenz et al., 2013). Further, even under similar abiotic stresses during the early growing season, new tissues tend to be more susceptible than in other growing stages (e.g., prolonged drought and heat stress), in particular for annual species such as most crops because other functional compartments (e.g., roots) are not fully developed (Lipiec et al., 2013; Wahid et al., 2007). Conversely, the recurrent stress-induced summer endodormancy (e.g., due to accumulated heat and drought) renders meristems insensitive to growing signals (Campoy et al., 2011; Cooke et al., 2012; Rohde & Bhalerao, 2007) may contribute to low mid-growing season anomalies.

Indeed, although both the mid and late-growing-season VI anomalies are comparatively small, the latter displays larger anomalies than the former. This may relate to the fact that autumn phenology tends to be sensitive to multiple growing conditions which can be highly variable. Autumn senescence is generally mostly driven by photoperiod and other light-related factors (Hänninen & Tanino, 2011; Way, 2011), but can also respond to temperature (L. Chen et al., 2020; Hänninen & Tanino, 2011; Richardson et al., 2018; Way, 2011; Wu et al., 2018), water availability (e.g., Sade et al., 2018), ambient CO_2 concentrations (Taylor et al., 2008), or the timing of spring leaf-out (Fu et al., 2014; Keenan & Richardson, 2015).

Alternatively, the dominance of early growing season anomalies might also be linked to the higher level of phenological synchronicity. Compared with fruit ripening, fruit harvesting, and leaf senescence, the changes of the timing for leaf unfolding are more consistent across species in response to changes in climate. For example, leaf unfolding exhibits a lower variance of sensitivity to temperature than leaf fall (Gordo & Sanz, 2009; Menzel et al., 2006; Peñuelas et al., 2002). Such differences in phenological synchronicity can lead to a more spatially consistent signal of greenness for the early growing season than for the other growing season months within a given gridpoint, as detected by satellites. The varied

response of leaf senescence across species may produce contrasting sub-grid signals that average out when spatially aggregated. This in turn implies that high-diversity ecosystems may exhibit larger cancellation effects in the late-growing season, and may thus appear to have weaker late-growing season anomalies, potentially resulting in a larger early- versus late-growing season difference than low-diversity ecosystems. The expected increase in plant phenological synchronicity (Wang et al., 2016) and changes in plant community composition in a changing climate (Hickler et al., 2012) may alter the observed level of phenological synchronicity among species and thus affect our understanding of future climate-vegetation coupling.

In addition to the aforementioned direct effects on plant physiology and community ecology, the dominance of early growing season variations can also be a consequence of indirect effects from local physical environments (e.g., recharging spring/summer soil moisture from winter precipitation, Barriopedro et al., 2006), and/or changes in pre-season conditions, which can be carried on to the current growing season. Furthermore, nutrient resorption related to leaf senescence at the end of the previous growing season could affect nutrient availability during the early growing season of the current year (Estiarte & Peñuelas, 2015).

As a consequence of these processes, vegetation responses during the early growing season can reflect climate variability over a wider temporal window than other growing season months. Indeed, the concurrent correlations between early-growing season NAO and early-growing season phenology (i.e., lag 0 months) are generally much weaker than the dominant asynchronous coupling (i.e., lag 1–2 months) we identified (Figure 7), in agreement with Gong and Ho (2003). Similar correlations have been found between the pre-season NAO and early-growing season phenology as measured by growing season onset (the timing of phenological phases instead of greenness anomalies investigated in this study), in particular in the deciduous and evergreen forests in the Baltic region (Aasa et al., 2004; Nordli et al., 2008). This is also in agreement with the large-scale results based on AVHRR NDVI (Gouveia et al., 2008; Maignan et al., 2008; Stöckli & Vidale, 2004).

Based on this evidence, the identified strong asynchronous coupling between teleconnection indices and vegetation indices can be explained by the effects of atmospheric dynamics on both physiological and ecological responses. Therefore, in principle, asynchronous coupling should not be limited to NAO, but may also apply to other large-scale circulation drivers. The coupling with the pre-season SCA and EA (lag 2 and lag 5 months, respectively) are good examples of these lagged effects. The negative impacts of pre-growing season SCA over central and southern Europe may relate to changes in cold air mass advection to southeastern Europe, affecting local winter and spring temperatures (Macias-Fauria et al., 2012; Vihma et al., 2020). A positive winter EA generally coincides with a cold winter (Comas-Bru & McDermott, 2014), which could increase snow depth and surface albedo for the early spring, leading to lower surface air temperature (T. Zhang, 2005). These pre-season changes may thus affect temperature-sensitive phenology, such as delaying the bud burst and leaf unfolding caused by changes in air or soil temperature. Moreover, cold winter in Scandinavia, as reflected by a negative NAO pattern, can cause higher snow cover and hence higher soil water supply in June–July in this region (Barriopedro et al., 2006), which in turn may prompt summer vegetation growth. However, we find a very limited NAO impact on summer phenology, which may require further investigation.

The teleconnection indices discussed here can be closely related to changes in atmospheric circulation. For example, the NAO has been related to the position and strength of the North Atlantic jet stream (Messori & Caballero, 2015; Woollings & Blackburn, 2012; Woollings et al., 2010) and the Southern Föhn flow in the Alps (Desai et al., 2016). To examine the mechanistic link between the teleconnection indices, European climate, and vegetation phenology, we conducted a preliminary analysis of the link between the pre-season 500 hPa geopotential height anomalies and the early-GS continental-scale VI anomalies. A close correspondence emerged between the 500 hPa geopotential height anomaly pattern associated with positive VI values in the boreal and temperate regions of Europe and the combination of positive NAO and negative SCA phases (not shown). This result supports the hypothesis that the relation between teleconnection indices and vegetation is mediated by anomalies in the Euro-Atlantic atmospheric circulation. Previous work has further shown that in the pre-season a positive NAO combined with a negative SCA is usually followed

by warm early-GS anomalies (Comas-Bru & McDermott, 2014), which could, in turn, promote leaf unfolding and positive VI anomalies.

Regarding the sensitivity of SOS and EOS to the local climate, our findings partly reflect some well-established features of climate-vegetation coupling, for example, the strong vegetation-temperature coupling during the early growing season over high-latitude Europe (Chmielewski & Rötzer, 2001; Menzel et al., 2006), and the vegetation-soil-moisture coupling during the late-growing season over central and southern Europe (e.g., Jongen et al., 2011). Moreover, we identify a large, albeit patchy, area across central and parts of northern Europe as being controlled by temperature during the late growing season (Figures S6b and S7h–S7l). This partly supports the findings from ecosystem-warming field experiments, in which the autumn senescence was in general delayed as ambient temperatures rose, but differed considerably among species (e.g., Richardson et al., 2018). The overall homogeneous control of photoperiod on the late-growing season greenness variation identified over the Scandinavian area (Figures 4 and S6) also supports recent findings using NDVI and solar-induced chlorophyll fluorescence (Y. Zhang et al., 2020).

From a methodological point of view, we note that our analysis of vegetation greenness relies on remote-sensing derived VI products, each with its own uncertainties. Sensor shifts can lead to artificial breaks in the long-term VI time-series (e.g., Tian et al., 2015), and the analysis period in our study may cover 1–2 sensor shifts corresponding to 1–2 breaks in the EVI2 time-series. However, these are expected to have a limited effect on the correlation coefficients. To test if the choice of VI products affects our results, we conducted the same VI-climate analyses employing an alternative satellite retrieval product, VIP-NDVI. Compared with GIMMS-NDVI and VIP-EVI2, VIP-NDVI differs in the remote-sensing platform from the former (MODIS vs. AVHRR, see Table 1) and differs in VI definition from the latter (NDVI vs. EVI2). We found that the differences between GIMMS-NDVI and VIP-NDVI are larger than the difference between VIP-NDVI and VIP-EVI2 (Figure S8), indicating that the sensor-induced bias tends to be more important than the VI-definition-induced bias for the VI-climate coupling analysis.

Moreover, we tested the robustness of our findings to the chosen spatial resolution of the data. We specifically tested using data at a higher resolution of 0.25°. We used the same datasets as in our main analysis, except that the number of frost days is calculated based on the daily minimum temperature derived from hourly ERA5 data, and 2m temperature, shortwave radiation, and soil moisture are at the original spatial resolutions instead of 0.5°. VIP-EVI2 is regridded to 0.25°. The overall coupling spatial pattern remains unchanged, yet the coupling strengths are slightly weaker for the 0.25° data than for the 0.5° data (Figure S9). This is partly expected because the higher resolution data set contains more small-scale noise that will partly confound the large-scale signal.

Finally, we also considered the impacts of the choice of VI smoothing approaches (Figure S3), phenological parameter settings (i.e., the threshold between 10% and 25% for SOS and EOS), and data temporal resolutions (e.g., monthly vs. daily, not shown) on the defined growing season. We found that the influences on the final outcome were limited.

5. Conclusions

We investigated the climate-vegetation coupling in Europe, based on two vegetation indices, local growing conditions, and seven teleconnection indices. We specifically considered a grid-wise definition of the growing season. We found that the coupling of climatic conditions and greenness anomalies during the first two months of the growing season largely determine those of the full growing season. NAO, SCA, and EA emerged as the most relevant large-scale drivers for this coupling. The relevance of the early part of the growing season on the changes in climate-vegetation coupling clearly shows the importance of locally identifying the timing of the growing season, in particular over large geographical domains, as opposed to using a coarser definition of the growing season based on fixed ranges of astronomical months.

Data Availability Statement

GIMMS NDVI3g (doi.org/10.3390/rs6086929) is available from: https://icdc.cen.uni-hamburg.de/en/gimms-ndvi3g.html. VIP15v004 EVI2 (https://doi.org/10.5067/MEaSUREs/VIP/VIP15.004) is available from: https://lpdaac.usgs.gov/products/vip15v004/. The MODIS landclass dataset MCD12C1 (DOI: 10.5067/MODIS/MCD12C1.006) is available from: https://lpdaac.usgs.gov/products/mcd12c1v006/. ERA5 reanalysis data (https://doi.org/10.24381/cds.f17050d7) is available from: https://cds.climate.copernicus.eu/cdsapp#!/dataset/reanalysis-era5-single-levels-monthly-means?tab=overview. CRU TS404 (doi.org/10.1038/s41597-020-0453-3) is available from: https://crudata.uea.ac.uk/cru/data/hrg/cru_ts_4.04/. The Global Land Evaporation Amsterdam Model (GLEAM) output (https://doi.org/10.5194/gmd-10-1903-2017, 2017) is available from: https://www.gleam.eu/. The teleconnection indices (https://doi.org/10.1126/science.269.5224.676) are available from: https://www.cpc.ncep.noaa.gov/data/teledoc/telecontents.shtml.

References

Aasa, A., Jaagus, J., Ahas, R., & Sepp, M. (2004). The influence of atmospheric circulation on plant phenological phases in central and eastern Europe. *International Journal of Climatology*, *24*(12), 1551–1564. https://doi.org/10.1002/joc.1066

Agoston, G. A. (1987). Color Specification (CIE). In G. A. Agoston Ed., *Color theory and its Application in Art and Design* (pp. 47–65). Springer Berlin Heidelberg. https://doi.org/10.1007/978-3-540-34734-7_6

Anderegg, W. R. L., Ballantyne, A. P., Smith, W. K., Majkut, J., Rabin, S., Beaulieu, C., et al. (2015). Tropical nighttime warming as a dominant driver of variability in the terrestrial carbon sink. *Proceedings of the National Academy of Sciences of the United States of America*, *112*(51), 15591–15596. https://doi.org/10.1073/pnas.1521479112

Augspurger, C. K. (2009). Spring 2007 warmth and frost: Phenology, damage and refoliation in a temperate deciduous forest. *Functional Ecology*, *23*(6), 1031–1039. https://doi.org/10.1111/j.1365-2435.2009.01587.x

Barichivich, J., Briffa, K. R., Myneni, R. B., Osborn, T. J., Melvin, T. M., Ciais, P., et al. (2013). Large-scale variations in the vegetation growing season and annual cycle of atmospheric CO_2 at high northern latitudes from 1950 to 2011. *Global Change Bioogy*, *19*(10), 3167–3183. https://doi.org/10.1111/gcb.12283

Barriopedro, D., García-Herrera, R., & Hernández, E. (2006). The role of snow cover in the Northern Hemisphere winter to summer transition. *Geophysical Research Letters*, *33*(14), 661. https://doi.org/10.1029/2006gl025763

Bastos, A., Janssens, I. A., Gouveia, C. M., Trigo, R. M., Ciais, P., Chevallier, F., et al. (2016). European land CO_2 sink influenced by NAO and East-Atlantic pattern coupling. *Nature Communications*, *7*, 10315. https://doi.org/10.1038/ncomms10315

Beck, P. S. A., Atzberger, C., Høgda, K. A., Johansen, B., & Skidmore, A. K. (2006). Improved monitoring of vegetation dynamics at very high latitudes: A new method using MODIS NDVI. *Remote Sensing of Environment*, *100*(3), 321–334. https://doi.org/10.1016/j.rse.2005.10.021

Behrenfeld, M. J., Randerson, J. T., McClain, C. R., Feldman, G. C., Los, S. O., Tucker, C. J., et al. (2001). Biospheric primary production during an ENSO transition. *Science*, *291*(5513), 2594–2597. https://doi.org/10.1126/science.1055071

Belmecheri, S., Babst, F., Hudson, A. R., Betancourt, J., & Trouet, V. (2017). Northern hemisphere jet stream position indices as diagnostic tools for climate and ecosystem dynamics. *Earth Interactions*, *21*(8), 1–23. https://doi.org/10.1175/ei-d-16-0023.1

Betts, R. A., Cox, P. M., Collins, M., Harris, P. P., Huntingford, C., & Jones, C. D. (2004). The role of ecosystem-atmosphere interactions in simulated Amazonian precipitation decrease and forest dieback under global climate warming. *Theoretical and Applied Climatology*, *78*(1), 157–175. https://doi.org/10.1007/s00704-004-0050-y

Bowman, K. W., Liu, J., Bloom, A. A., Parazoo, N. C., Lee, M., Jiang, Z., et al. (2017). Global and Brazilian carbon response to El Niño Modoki 2011-2010. *Earth and Space Science*, *4*(10), 637–660. https://doi.org/10.1002/2016ea000204

Cai, Z., Jönsson, P., Jin, H., & Eklundh, L. (2017). Performance of smoothing methods for reconstructing NDVI time-series and estimating vegetation phenology from MODIS data. *Remote Sensing*, *9*(12), 1271. https://doi.org/10.3390/rs9121271

Campoy, J. A., Ruiz, D., & Egea, J. (2011). Dormancy in temperate fruit trees in a global warming context: A review. *Scientia Horticulturae*, *130*(2), 357–372. https://doi.org/10.1016/j.scienta.2011.07.011

Chen, L., Hänninen, H., Rossi, S., Smith, N. G., Pau, S., Liu, Z., et al. (2020). Leaf senescence exhibits stronger climatic responses during warm than during cold autumns. *Nature Climate Change*, *10*(8), 777–780. https://doi.org/10.1038/s41558-020-0820-2

Chen, Z. M., Babiker, I. S., Chen, Z. X., Komaki, K., Mohamed, M. A. A., & Kato, K. (2004). Estimation of interannual variation in productivity of global vegetation using NDVI data. *International Journal of Remote Sensing*, *25*(16), 3139–3159. https://doi.org/10.1080/0143116032000160435

Chmielewski, F.-M., & Rötzer, T. (2001). Response of tree phenology to climate change across Europe. *Agricultural and Forest Meteorology*, *108*(2), 101–112. https://doi.org/10.1016/s0168-1923(01)00233-7

Ciais, P., Sabine, C., Bala, G., Bopp, L., Brovkin, V., Canadell, J., et al. (2013). *Carbon and other biogeochemical cycles. Climate change 2013: The physical science basis. Contribution of working group I to the Fifth Assessment Report of the Intergovernmental panel on climate change* (pp. 465–570). Cambridge, UK; New York, NY: Cambridge University Press.

Comas-Bru, L., & McDermott, F. (2014). Impacts of the EA and SCA patterns on the European twentieth century NAO-winter climate relationship. *Quarterly Journal of the Royal Meteorological Society*, *140*(679), 354–363. https://doi.org/10.1002/qj.2158

Cooke, J. E. K., Eriksson, M. E., & Junttila, O. (2012). The dynamic nature of bud dormancy in trees: Environmental control and molecular mechanisms. *Plant, Cell and Environment*, *35*(10), 1707–1728. https://doi.org/10.1111/j.1365-3040.2012.02552.x

Desai, A. R., Wohlfahrt, G., Zeeman, M. J., Katata, G., Eugster, W., Montagnani, L., et al. (2016). Montane ecosystem productivity responds more to global circulation patterns than climatic trends. *Environmental Research Letters*, *11*(2). 024013. https://doi.org/10.1088/1748-9326/11/2/024013

Didan, K. (2010). Multi-satellite earth science data record for studying global vegetation trends and changes. In *Proceedings of the 2010 International Geoscience and Remote Sensing Symposium, Honolulu, HI, USA* (Vol. *2530*, p. 2530). Retrieved from https://measures.arizona.edu/documents/dataviewer/K_Didan_IGARSS_2010.pdf

Estiarte, M., & Peñuelas, J. (2015). Alteration of the phenology of leaf senescence and fall in winter deciduous species by climate change: Effects on nutrient proficiency. *Global Change Biology*, *21*(3), 1005–1017. https://doi.org/10.1111/gcb.12804

FAO. (2020). *Earth observation*. Retrieved October 24, 2020, from http://www.fao.org/giews/earthobservation/asis/index_1.jsp?lang=en

Friedlingstein, P., Cox, P., Betts, R., Bopp, L., von Bloh, W., Brovkin, V., et al. (2006). Climate-carbon cycle feedback analysis: Results from the C4MIP model intercomparison. *Journal of Climate*, *19*(14), 3337–3353. https://doi.org/10.1175/jcli3800.1

Friedlingstein, P., Jones, M., O'sullivan, M., Andrew, R. M., Hauck, J., Peters, G. P., et al. (2019). Global carbon budget 2019. *Earth System Science Data*, *11*(4), 1783–1838

Friedl, M. A., McIver, D. K., Hodges, J. C. F., Zhang, X. Y., Muchoney, D., Strahler, A. H., et al. (2002). Global land cover mapping from MODIS: Algorithms and early results. *Remote Sensing of Environment*, *83*(1), 287–302. https://doi.org/10.1016/s0034-4257(02)00078-0

Fu, Y. H., Piao, S., Op de Beeck, M., Cong, N., Zhao, H., Zhang, Y., et al. (2014). Recent spring phenology shifts in western Central Europe based on multiscale observations. *Global Ecology and Biogeography*, *23*(11), 1255–1263. https://doi.org/10.1111/geb.12210

Gao, F., Morisette, J. T., Wolfe, R. E., Ederer, G., Pedelty, J., Masuoka, E., et al. (2008). An algorithm to produce temporally and spatially continuous MODIS-LAI time series. *IEEE Geoscience and Remote Sensing Letters*, *5*(1), 60–64. https://doi.org/10.1109/lgrs.2007.907971

Gong, D.-Y., & Ho, C.-H. (2003). Detection of large-scale climate signals in spring vegetation index (normalized difference vegetation index) over the Northern Hemisphere. *Journal of Geophysical Research - D: Atmospheres*, *108*(D16). https://doi.org/10.1029/2002jd002300

Gonsamo, A., Chen, J. M., & Lombardozzi, D. (2016). Global vegetation productivity response to climatic oscillations during the satellite era. *Global Change Biology*, *22*(10), 3414–3426. https://doi.org/10.1111/gcb.13258

Gonsamo, A., Chen, J. M., Price, D. T., Kurz, W. A., & Wu, C. (2012). Land surface phenology from optical satellite measurement and CO_2 eddy covariance technique. *Journal of Geophysical Research: Biogeosciences*, *117*(G3). https://doi.org/10.1029/2012jg002070

Gordo, O., & Sanz, J. J. (2009). Long-term temporal changes of plant phenology in the Western Mediterranean. *Global Change Biology*, *15*(8), 1930–1948. Retrieved from https://doi.org/10.1111/j.1365-2486.2009.01851.x

Goulden, M. L., Wofsy, S. C., Harden, J. W., Trumbore, S. E., Crill, P. M., Gower, S. T., et al. (1998). Sensitivity of boreal forest carbon balance to soil thaw. *Science*, *279*(5348), 214–217. https://doi.org/10.1126/science.279.5348.214

Gouveia, C., Trigo, R. M., DaCamara, C. C., Libonati, R., & Pereira, J. M. C. (2008). The North Atlantic oscillation and European vegetation dynamics. *International Journal of Climatology*, *28*(14), 1835–1847. https://doi.org/10.1002/joc.1682

Hänninen, H., & Tanino, K. (2011). Tree seasonality in a warming climate. *Trends in Plant Science*, *16*(8), 412–416. https://doi.org/10.1016/j.tplants.2011.05.001

Harris, I., Osborn, T. J., Jones, P., & Lister, D. (2020). Version 4 of the CRU TS monthly high-resolution gridded multivariate climate dataset. *Scientific Data*, *7*(1), 109. https://doi.org/10.1038/s41597-020-0453-3

Hersbach, H., Bell, B., Berrisford, P., Hirahara, S., Horányi, A., Muñoz-Sabater, J., et al. (2020). The ERA5 global reanalysis. *Quarterly Journal of the Royal Meteorological Society*, *146*(730), 1999–2049. https://doi.org/10.1002/qj.3803

Hickler, T., Vohland, K., Feehan, J., Miller, P. A., Smith, B., Costa, L., et al. (2012). Projecting the future distribution of European potential natural vegetation zones with a generalized, tree species-based dynamic vegetation model. *Global Ecology and Biogeography: A Journal of Macroecology*, *21*(1), 50–63. https://doi.org/10.1111/j.1466-8238.2010.00613.x

Homyak, P. M., Blankinship, J. C., Slessarev, E. W., Schaeffer, S. M., Manzoni, S., & Schimel, J. P. (2018). Effects of altered dry season length and plant inputs on soluble soil carbon. *Ecology*, *99*(10), 2348–2362. https://doi.org/10.1002/ecy.2473

Hurrell, J. W., & Deser, C. (2010). North Atlantic climate variability: The role of the North Atlantic Oscillation. *Journal of Marine Systems*, *79*(3), 231–244. https://doi.org/10.1016/j.jmarsys.2009.11.002

Hurrell, J. W., Kushnir, Y., & Visbeck, M. (2001). CLIMATE: The North Atlantic oscillation. *Science*, *291*(5504), 603–605. https://doi.org/10.1126/science.1058761

Jarvis, P., Rey, A., Petsikos, C., Wingate, L., Rayment, M., Pereira, J., et al. (2007). Drying and wetting of Mediterranean soils stimulates decomposition and carbon dioxide emission: The "Birch effect". *Tree Physiology*, *27*(7), 929–940. https://doi.org/10.1093/treephys/27.7.929

Jeong, S.-J., Ho, C.-H., Gim, H.-J., & Brown, M. E. (2011). Phenology shifts at start vs. end of growing season in temperate vegetation over the Northern Hemisphere for the period 1982-2008. *Global Change Biology*, *17*(7), 2385–2399. https://doi.org/10.1111/j.1365-2486.2011.02397.x

Jiang, Z., Huete, A., Didan, K., & Miura, T. (2008). Development of a two-band enhanced vegetation index without a blue band. *Remote Sensing of Environment*, *112*(10), 3833–3845. https://doi.org/10.1016/j.rse.2008.06.006

Jin, H., Jönsson, A. M., Olsson, C., Lindström, J., Jönsson, P., & Eklundh, L. (2019). New satellite-based estimates show significant trends in spring phenology and complex sensitivities to temperature and precipitation at northern European latitudes. *International Journal of Biometeorology*, *63*(6), 763–775. https://doi.org/10.1007/s00484-019-01690-5

Jongen, M., Pereira, J. S., Aires, L. M. I., & Pio, C. A. (2011). The effects of drought and timing of precipitation on the inter-annual variation in ecosystem-atmosphere exchange in a Mediterranean grassland. *Agricultural and Forest Meteorology*, *151*(5), 595–606. https://doi.org/10.1016/j.agrformet.2011.01.008

Jönsson, P., & Eklundh, L. (2004). TIMESAT-a program for analyzing time-series of satellite sensor data. *Computers & Geosciences*, *30*(8), 833–845. https://doi.org/10.1016/j.cageo.2004.05.006

Kang, Y., Özdoğan, M., Zipper, S., Román, M., Walker, J., Hong, S., et al. (2016). How universal is the relationship between remotely sensed vegetation indices and crop leaf area index? A global assessment. *Remote Sensing*, *8*(7), 597. https://doi.org/10.3390/rs8070597

Keeling, C. D., Whorf, T. P., Wahlen, M., & van der Plichtt, J. (1995). Interannual extremes in the rate of rise of atmospheric carbon dioxide since 1980. *Nature*, *375*(6533), 666–670. https://doi.org/10.1038/375666a0

Keenan, T. F., & Richardson, A. D. (2015). The timing of autumn senescence is affected by the timing of spring phenology: Implications for predictive models. *Global Change Biology 21*(7), 2634–2641. https://doi.org/10.1111/gcb.12890

Kottek, M., Grieser, J., Beck, C., Rudolf, B., & Rubel, F. (2006). World Map of the Köppen-Geiger climate classification updated. *Metz*, *15*(3), 259–263. https://doi.org/10.1127/0941-2948/2006/0130

Law, B. E., Falge, E., Gu, L., Baldocchi, D. D., Bakwin, P., Berbigier, P., et al. (2002). Environmental controls over carbon dioxide and water vapor exchange of terrestrial vegetation. *Agricultural and Forest Meteorology*, *113*(1), 97–120. https://doi.org/10.1016/s0168-1923(02)00104-1

Lenz, A., Hoch, G., Vitasse, Y., & Körner, C. (2013). European deciduous trees exhibit similar safety margins against damage by spring freeze events along elevational gradients. *New Phytologist*, *200*(4), 1166–1175. https://doi.org/10.1111/nph.12452

Le Quéré, C., Andrew, R. M., Friedlingstein, P., Sitch, S., Hauck, J., Pongratz, J., et al. (2018). Global Carbon Budget 2018. *Earth System Science Data*, *10*(4), 2141–2194. https://doi.org/10.5194/essd-10-2141-2018

Linderholm, H. W. (2006). Growing season changes in the last century. *Agricultural and Forest Meteorology*, *137*(1), 1–14. https://doi.org/10.1016/j.agrformet.2006.03.006

Lipiec, J., Doussan, C., Nosalewicz, A., & Kondracka, K. (2013). Effect of drought and heat stresses on plant growth and yield: A review. *International Agrophysics*, *27*(4). https://doi.org/10.2478/intag-2013-0017

Liu, J., Pattey, E., & Jégo, G. (2012). Assessment of vegetation indices for regional crop green LAI estimation from Landsat images over multiple growing seasons. *Remote Sensing of Environment*, *123*, 347–358. https://doi.org/10.1016/j.rse.2012.04.002

Macias-Fauria, M., Forbes, B. C., Zetterberg, P., & Kumpula, T. (2012). Eurasian Arctic greening reveals teleconnections and the potential for structurally novel ecosystems. *Nature Climate Change*, *2*(8), 613–618. https://doi.org/10.1038/nclimate1558

Maignan, F., Bréon, F.-M., Bacour, C., Demarty, J., & Poirson, A. (2008). Interannual vegetation phenology estimates from global AVHRR measurements. *Remote Sensing of Environment*, *112*(2), 496–505. https://doi.org/10.1016/j.rse.2007.05.011

Martens, B., Miralles, D. G., Lievens, H., van der Schalie, R., de Jeu, R. A. M., Fernández-Prieto, D., et al. (2017). GLEAM v3: Satellite-based land evaporation and root-zone soil moisture. *Geoscientific Model Development*, *10*(5), 1903–1925. https://doi.org/10.5194/gmd-10-1903-2017

Menzel, A., & Fabian, P. (1999). Growing season extended in Europe. *Nature*, *397*(6721), 659659. https://doi.org/10.1038/17709

Menzel, A., Sparks, T. H., Estrella, N., Koch, E., Aasa, A., Ahas, R., et al. (2006). European phenological response to climate change matches the warming pattern. *Global Change Biology*, *12*(10), 1969–1976. https://doi.org/10.1111/j.1365-2486.2006.01193.x

Messori, G., & Caballero, R. (2015). On double Rossby wave breaking in the North Atlantic: DOUBLE ROSSBY WAVE BREAKING. *Journal of Geophysical Research*, *120*(21). 11129–11150. https://doi.org/10.1002/2015jd023854

Messori, G., Ruiz-Pérez, G., Manzoni, S., & Vico, G. (2019). Climate drivers of the terrestrial carbon cycle variability in Europe. *Environmental Research Letters*, *14*(6). 063001. https://doi.org/10.1088/1748-9326/ab1ac0

Miralles, D. G., Holmes, T. R. H., De Jeu, R. A. M., Gash, J. H., Meesters, A. G. C. A., & Dolman, A. J. (2011). Global land-surface evaporation estimated from satellite-based observations. *Hydrology and Earth System Sciences*, *15*(2), 453–469. https://doi.org/10.5194/hess-15-453-2011

Morales, P., Hickler, T., Rowell, D. P., Smith, B., & Sykes, M. T. (2007). Changes in European ecosystem productivity and carbon balance driven by regional climate model output. *Global Change Biology*, *13*(1), 108–122. https://doi.org/10.1111/j.1365-2486.2006.01289.x

Moser, L., Fonti, P., Büntgen, U., Esper, J., Luterbacher, J., Franzen, J., & Frank, D. (2010). Timing and duration of European larch growing season along altitudinal gradients in the Swiss Alps. *Tree Physiology*, *30*(2), 225–233. https://doi.org/10.1093/treephys/tpp108

Noormets, A., McNulty, S. G., DeForest, J. L., Sun, G., Li, Q., & Chen, J. (2008). Drought during canopy development has lasting effect on annual carbon balance in a deciduous temperate forest. *New Phytologist*, *179*(3), 818–828. https://doi.org/10.1111/j.1469-8137.2008.02501.x

Nordli, Ø., Wielgolaski, F. E., Bakken, A. K., Hjeltnes, S. H., Måge, F., Sivle, A., & Skre, O. (2008). Regional trends for bud burst and flowering of woody plants in Norway as related to climate change. *International Journal of Biometeorology*, *52*(7), 625–639. https://doi.org/10.1007/s00484-008-0156-5

Novick, K. A., Ficklin, D. L., Stoy, P. C., Williams, C. A., Bohrer, G., Oishi, A. C., et al. (2016). The increasing importance of atmospheric demand for ecosystem water and carbon fluxes. *Nature Climate Change*, *6*(11), 1023–1027. https://doi.org/10.1038/nclimate3114

Olsson, P.-O., Kantola, T., Lyytikäinen-Saarenmaa, P., Jönsson, A. M., & Eklundh, L. (2016). Development of a method for monitoring of insect induced forest defoliation-limitation of MODIS data in Fennoscandian forest landscapes. *Silva Fennica*. *50*(2).

Peñuelas, J., Filella, I., & Comas, P. (2002). Changed plant and animal life cycles from 1952 to 2000 in the Mediterranean region. *Global Change Biology*, *8*(6), 531–544. https://doi.org/10.1046/j.1365-2486.2002.00489.x

Pedelty, J., Devadiga, S., Masuoka, E., Brown, M., Pinzon, J., Tucker, C., et al. (2007). Generating a Long-term Land Data Record from the AVHRR and MODIS Instruments. In *2007 IEEE international Geoscience and remote sensing Symposium* (pp. 1021–1025). https://doi.org/10.1109/IGARSS.2007.4422974

Piao, S., Liu, Q., Chen, A., Janssens, I. A., Fu, Y., Dai, J., et al. (2019). Plant phenology and global climate change: Current progresses and challenges. *Global Change Biology*, *25*(6), 1922–1940. https://doi.org/10.1111/gcb.14619

Piao, S., Wang, X., Wang, K., Li, X., Bastos, A., Canadell, J. G., et al. (2020). Interannual variation of terrestrial carbon cycle: Issues and perspectives. *Global Change Biology*, *26*(1), 300–318. https://doi.org/10.1111/gcb.14884

Pinzon, J., & Tucker, C. (2014). A Non-Stationary 1981-2012 AVHRR NDVI3g Time Series. *Remote Sensing*, *6*(8), 6929–6960. https://doi.org/10.3390/rs6086929

Qian, H., Joseph, R., & Zeng, N. (2008). Response of the terrestrial carbon cycle to the El Niˉno-Southern Oscillation. *Tellus B: Chemical and Physical Meteorology*, *60*(4), 537–550. https://doi.org/10.1111/j.1600-0889.2008.00360.x

Rasmusson, E. M., & Wallace, J. M. (1983). Meteorological aspects of the el nino/southern oscillation. *Science*, *222*(4629), 1195–1202. https://doi.org/10.1126/science.222.4629.1195

Reed, B. C., Brown, J. F., VanderZee, D., Loveland, T. R., Merchant, J. W., & Ohlen, D. O. (1994). Measuring phenological variability from satellite imagery. *Journal of Vegetation Science: Official Organ of the International Association for Vegetation Science*, *5*(5), 703–714. https://doi.org/10.2307/3235884

Reuter, M., Buchwitz, M., Hilker, M., Heymann, J., Bovensmann, H., Burrows, J. P., et al. (2017). How Mmuch CO_2 is taken up by the European terrestrial biosphere? *Bulletin of the American Meteorological Society*, *98*(4), 665–671. https://doi.org/10.1175/bams-d-15-00310.1

Richardson, A. D., Andy Black, T., Ciais, P., Delbart, N., Friedl, M. A., Gobron, N., et al. (2010). Influence of spring and autumn phenological transitions on forest ecosystem productivity. *Philosophical Transactions of the Royal Society B*, *365*(1555), 3227–3246. https://doi.org/10.1098/rstb.2010.0102

Richardson, A. D., Hufkens, K., Milliman, T., Aubrecht, D. M., Furze, M. E., Seyednasrollah, B., et al. (2018). Ecosystem warming extends vegetation activity but heightens vulnerability to cold temperatures. *Nature*, *560*(7718), 368–371. https://doi.org/10.1038/s41586-018-0399-1

Rocha, A. V., & Shaver, G. R. (2009). Advantages of a two band EVI calculated from solar and photosynthetically active radiation fluxes. *Agricultural and Forest Meteorology*, *149*(9), 1560–1563. https://doi.org/10.1016/j.agrformet.2009.03.016

Rödenbeck, C., Zaehle, S., Keeling, R., Heimann, M., & Others (2018). *How does the terrestrial carbon exchange respond to inter-annual climatic variations?: A quantification based on atmospheric CO_2 data*. Biogeosciences . Retrieved from https://helda.helsinki.fi/handle/10138/278429

Rohde, A., & Bhalerao, R. P. (2007). Plant dormancy in the perennial context. *Trends in Plant Science*, *12*(5), 217–223. https://doi.org/10.1016/j.tplants.2007.03.012

Rötzer, T., & Chmielewski, F. (2001). Phenological maps of Europe. *Climate Research*, *18*(3), 249–257. https://doi.org/10.3354/cr018249

Rouse, J. W., Jr, Haas, R. H., Deering, D. W., & Schell, J. A. (1974). *NASA Technical Reports Server (NTRS)*. Retrieved October 13, 2020 from https://ntrs.nasa.gov/search.jsp?R=19750020419

Ruiz-Pérez, G., & Vico, G. (2020). Effects of temperature and water availability on Northern European Boreal forests. *Frontiers in Forests and Global Change*, *3*, 34. https://doi.org/10.3389/ffgc.2020.00034

Sade, N., Del Mar Rubio-Wilhelmi, M., Umnajkitikorn, K., & Blumwald, E. (2018). Stress-induced senescence and plant tolerance to abiotic stress. *Journal of Experimental Botany*, *69*(4), 845–853. https://doi.org/10.1093/jxb/erx235

Solberg, S. (2004). Summer drought: A driver for crown condition and mortality of Norway spruce in Norway. *Forest Pathology*, *34*(2), 93–104. https://doi.org/10.1111/j.1439-0329.2004.00351.x

Stöckli, R., & Vidale, P. L. (2004). European plant phenology and climate as seen in a 20-year AVHRR land-surface parameter dataset. *International Journal of Remote Sensing*, *25*(17), 3303–3330. https://doi.org/10.1080/01431160310001618149

Talmon, Y., Sternberg, M., & Grünzweig, J. M. (2011). Impact of rainfall manipulations and biotic controls on soil respiration in Mediterranean and desert ecosystems along an aridity gradient. *Global Change Biology*, *17*(2), 1108–1118. https://doi.org/10.1111/j.1365-2486.2010.02285.x

Taylor, G., Tallis, M. J., Giardina, C. P., Percy, K. E., Miglietta, F., Gupta, P. S., et al. (2008). Future atmospheric CO_2 leads to delayed autumnal senescence. *Global Change Biology*, *14*(2), 264–275. https://doi.org/10.1111/j.1365-2486.2007.01473.x

Thompson, R., & Clark, R. M. (2008). Is spring starting earlier? *The Holocene*, *18*(1), 95–104. https://doi.org/10.1177/0959683607085599

Tian, F., Fensholt, R., Verbesselt, J., Grogan, K., Horion, S., & Wang, Y. (2015). Evaluating temporal consistency of long-term global NDVI datasets for trend analysis. *Remote Sensing of Environment*, *163*, 326–340. https://doi.org/10.1016/j.rse.2015.03.031

Tucker, C. J., Pinzon, J. E., Brown, M. E., Slayback, D. A., Pak, E. W., Mahoney, R., et al. (2005). An extended AVHRR 8-km NDVI dataset compatible with MODIS and SPOT vegetation NDVI data. *International Journal of Remote Sensing*, *26*(20), 4485–4498. https://doi.org/10.1080/01431160500168686

Vermote, E., Saleous, N. E. L., Kaufman, Y. J., & Dutton, E. (1997). Data pre-processing: Stratospheric aerosol perturbing effect on the remote sensing of vegetation: Correction method for the composite NDVI after the Pinatubo eruption. *Remote Sensing Reviews*, *15*(1–4), 7–21. https://doi.org/10.1080/02757259709532328

Vihma, T., Graversen, R., Chen, L., Handorf, D., Skific, N., Francis, J. A., et al. (2020). Effects of the tropospheric large-scale circulation on European winter temperatures during the period of amplified Arctic warming. *International Journal of Climatology*, *40*(1), 509–529. https://doi.org/10.1002/joc.6225. https://doi.org/10.1002/joc.6225

Wahid, A., Gelani, S., Ashraf, M., & Foolad, M. (2007). Heat tolerance in plants: An overview. *Environmental and Experimental Botany*, *61*(3), 199–223. https://doi.org/10.1016/j.envexpbot.2007.05.011

Wang, C., Tang, Y., & Chen, J. (2016). Plant phenological synchrony increases under rapid within-spring warming. *Scientific Reports*, *6*(1), 25460. https://doi.org/10.1038/srep25460

Way, D. A. (2011). Tree phenology responses to warming: spring forward, fall back? *Tree Physiology*, *31*(5), 469–471. https://doi.org/10.1093/treephys/tpr044

Woollings, T., & Blackburn, M. (2012). The North Atlantic jet stream under climate change and its relation to the NAO and EA patterns. *Journal of Climate*, *25*(3), 886–902. https://doi.org/10.1175/jcli-d-11-00087.1

Woollings, T., Hannachi, A., & Hoskins, B. (2010). Variability of the North Atlantic eddy-driven jet stream. *Quarterly Journal of the Royal Meteorological Society*, *136*(649), 856–868. https://doi.org/10.1002/qj.625

Wu, C., Wang, X., Wang, H., Ciais, P., Peñuelas, J., Myneni, R. B., et al. (2018). Contrasting responses of autumn-leaf senescence to daytime and night-time warming. *Nature Climate Change*, *8*(12), 1092–1096. https://doi.org/10.1038/s41558-018-0346-z

Zeng, N., Mariotti, A., & Wetzel, P. (2005). Terrestrial mechanisms of interannual CO_2 variability. *Global Biogeochemical Cycles*, *19*(1). https://doi.org/10.1029/2004gb002273

Zhang, T. (2005). Influence of the seasonal snow cover on the ground thermal regime: An overview. *Reviews of Geophysics*, *43*(4), 1. https://doi.org/10.1029/2004rg000157

Zhang, Y., Commane, R., Zhou, S., Williams, A. P., & Gentine, P. (2020). Light limitation regulates the response of autumn terrestrial carbon uptake to warming. *Nature Climate Change*, *10*(8), 739–743. https://doi.org/10.1038/s41558-020-0806-0